Article

# Straw-Derived Activated Carbon Decorated with Ag₃PO₄ for Organic Pollutant Removal by a Circular Degradation Mechanism: Adsorption and Photocatalysis

Yihang Yue,[#] Lin Han,[#] Bo Ding,[#] Yanxi Yang, Xiaoju Yue, Shifeng Wang,* Qingguo Song, and Chun Du*

Read Online

ACCESS | Metrics & More | Article Recommendations

**ABSTRACT:** The escalating problem of water pollution has become an urgent concern, as it significantly undermines people's quality of life and overall public health. The increasing severity of water pollution represents a global challenge, with profound implications for human society. In this study, hydrothermal carbonization coupled with alkaline activation was utilized to repurpose barley straw into activated carbon (AC) as an absorbent. Silver phosphate (Ag₃PO₄) was synthesized as a potent photocatalyst. Subsequent ultrasound-assisted loading integrated the robust adsorptive capabilities of the AC with the advanced photocatalytic efficiency of silver phosphate, resulting in a superior composite material (AC/Ag₃PO₄) and implementing a novel "absorption−photocatalysis" active circular degradation strategy to remove hazardous organics in water. Comprehensive characterization assays confirmed the successful synthesis and incorporation of Ag₃PO₄ onto the AC scaffold. The composite with a Ag₃PO₄ concentration of 3 wt % exhibited a high methylene blue (MB) removal efficiency of 99.4% within 100 min. The reaction rate of this composite surpassed that of standalone AC by a factor of 2.89. Furthermore, cyclic regeneration studies via adsorption−desorption methodologies revealed the composite's resilience and sustained performance. The MB removal efficiency was maintained at 85.5% over five consecutive cycles, demonstrating the composite's remarkable stability. The integration of adsorptive and photocatalytic functionalities within a single system mitigates potential secondary pollution arising during the AC's desorption phase and enhances the organic contaminant removal efficiency. Moreover, the utilization of this integrated material reduces the quantity of chemicals and energy required for conventional adsorption water treatment techniques, as the material harnesses sunlight or alternative light sources to catalyze contaminant decomposition. This reduces the dependence on chemical treatment agents, contributing to resource conservation and alleviating environmental burdens. This pioneering approach offers a novel paradigm for addressing pollutant challenges in aqueous environments.
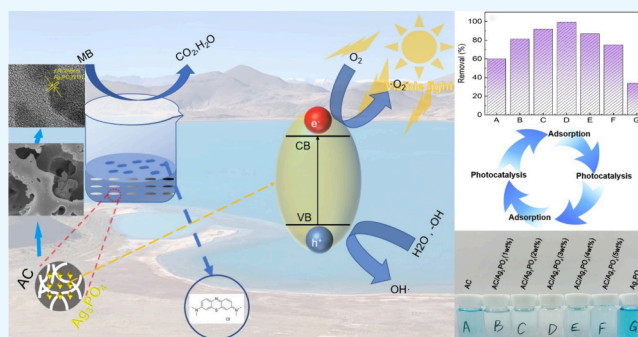
## 1. INTRODUCTION

Amid escalating industrialization, environmental degradation has intensified. The repercussions of water contamination on human health have become significantly detrimental, with a myriad of maladies traceable to polluted water sources. Certain dyes and their breakdown products, such as aromatic amines, exhibit strong carcinogenic properties. Numerous studies have investigated wastewater remediation. In response to this challenge, extensive research has been conducted on the use of photocatalysts, electrocatalysts, and various adsorption materials for the degradation of pollutants in water bodies.[1−4] This approach not only effectively enhances the efficiency of water purification but also significantly reduces negative environmental impacts. However, the expeditious and efficient removal of dye contaminants from water is a pressing challenge in modern environmental protection.

The methods for the removal of organic pollutants such as dyes have predominantly comprised physical modalities such as adsorption,[5,6] biological techniques such as biodegradation,[7−9] and chemical methodologies such as chlorination and ozonation.[10] Recent research has introduced innovative wastewater treatment techniques such as synergized coagulation, electrochemical oxidation, and activated sludge processes.[11−13,8,14−16] The various methods deployed for

sewage treatment have their own set of challenges. For instance, the physical adsorption technique possesses a finite adsorption capacity. Once the adsorbent medium is saturated, it requires replacement or regeneration. Moreover, this method might not be as effective for specific pollutants, which can lead to secondary contamination or escalate treatment expenses when the adsorbent requires regeneration. Similarly, biodegradation might not be as efficient for certain recalcitrant or toxic contaminants. Biodegradation requires meticulous maintenance of the biological community's stability, and its effectiveness is influenced by external factors such as temperature, pH, and nutrient levels. There is also the risk of generating secondary pollutants. Chemical treatments, especially those centered around chlorination and ozone, can produce harmful byproducts, such as trichloromethane and other halogenated organics. Treatment mentioned above also demands the addition of chemicals, which can inflate costs and might not be effective against all contaminants. A shared drawback across these methods is their potential to create secondary pollutant phases.[17]

In previous studies, barley straw was used to synthesize AC with superior adsorptive capabilities. This biomass-derived AC exhibits formidable adsorption potential against a diverse pollutant spectrum. Its adsorptive attributes, contingent on its preparative protocol, modulate its pore configuration and surface functional assemblages.[18−20] Despite the remarkable adsorption capabilities of biomass-derived AC toward dye organic contaminants, there is a concern about the potential for secondary pollution during its regeneration, owing to potential desorption. The sole adsorption capability of AC does not fully eliminate pollutants; it merely traps them within its pore structure. Thus, to achieve comprehensive pollutant removal, research has begun to shift toward photocatalytic materials.

In the realm of photocatalysts, a variety of materials are commonly available on the market, including titanium dioxide ($TiO_2$), zinc oxide (ZnO), cadmium sulfide (CdS), molybdenum disulfide ($MoS_2$), perovskite materials, and silver phosphate ($Ag_3PO_4$).[21−26] Among these, $Ag_3PO_4$ distinguishes itself with outstanding photocatalytic performance, considerable stability, a broad visible light response range, and ease of synthesis. These characteristics underscore its unique advantages over other materials, positioning $Ag_3PO_4$ as a focal point of research in the field of visible light photocatalysis. As is widely known, $Ag_3PO_4$, a visible-light-responsive photocatalyst, is known for its effectiveness in liberating oxygen from water and detoxifying the environment, attributable to its narrow bandgap (2.45 eV).[27,28] Its capabilities encompass both oxygen generation from aqueous systems and environmental purification. In practical applications of photocatalysts for pollutant degradation, the process is often accompanied by high costs associated with material preparation and operation, which limit its widespread use. Moreover, many degradation technologies perform well under laboratory conditions but experience a decrease in effectiveness in actual environments due to issues such as material agglomeration and challenges in regeneration. Additionally, factors like water quality and temperature can also impact performance.[29] For instance, in turbid water conditions, light cannot penetrate the water to reach the surface of the catalyst, significantly reducing the efficiency of photocatalysis.[30] A plethora of research has been undertaken to investigate the capabilities of activated carbon derived from various biomass and organic substances. Integrative studies utilizing nitrogen-doped graphitic carbon from phthalonitrile resin, persulfate-activated graphitic carbon nitride, and nickel-alloy decorated sucrose-derived carbon constructs have charted new courses for the development of environmentally friendly photocatalysts.[31−33] Notably, biochar-supported $CdS/TiO_2$ heterojunction photocatalysts have demonstrated exceptional aptitude for the selective photoconversion of glucose, concurrently generating hydrogen and organic acids.[34] These innovations pave the way for the integration of $Ag_3PO_4$ with activated carbon, culminating in innovative adsorptive photocatalytic composites. Such composites are poised to tackle the challenge of efficiently removing pollutants at high concentrations, a task that singular adsorbent and photocatalytic materials find formidable.

Empirical findings revealed that the $AC/Ag_3PO_4$ composites alleviated secondary contamination and enhanced the organic matter removal capacity of the material, resulting in an integrated adsorption−photocatalysis−adsorption cycle. Multiple assessments revealed the composite's proficiency in removing methylene blue (MB) from water. The formulation with 3 wt % $AC/Ag_3PO_4$ achieved a high removal efficiency of 99.4% within 100 min, which demonstrates the superior performance of the composite. The reaction rate of the composite was 2.89 times that of the standalone AC, demonstrating the rapid and potent reactive capability of the composite. However, this efficiency represents just a fraction of the broader merits of the composite. Successive cyclic regeneration studies via adsorption−desorption methodologies further demonstrated the stability and robustness of the composite. Even after undergoing five consecutive usage cycles, the composite maintained a removal efficiency of close to 85.5%, demonstrating its consistent performance and dependability over extended use. Moreover, the composite seamlessly integrates adsorption and photocatalysis within a single framework. This dual functionality provides a robust solution to recurrent secondary pollution issues in wastewater treatment and reduces dependency on chemical agents. The $AC/Ag_3PO_4$ blend, by synergistically utilizing both matrices, initiates and integrated adsorption−photocatalysis−adsorption cycle, thereby contributing positively to environmental improvement. Compared to related studies on the removal of low-concentration MB,[35,36] the $AC/Ag_3PO_4$ composite material demonstrated a removal capacity and excellent recyclability that were not inferior to those studies, even under high-concentration MB solutions (200 mg/L). This is attributed to the presence of a meticulously designed adsorption−photocatalysis self-cycle system within the composite material. In summary, this avant-garde methodology allows for addressing prevailing waterborne pollutant challenges, indicating promising avenues for future research and practical applications.

## 2. MATERIALS AND METHODS

**2.1. Materials.** The following were acquired from commercial sources: citric acid (≥99.5%, sample purchased from Aladdin), potassium hydroxide (99.99%, sample purchased from Aladdin), phosphoric acid (≥99.5%, sample purchased from Aladdin), potassium dichromate (≥99.8%, sample purchased from Chengdu Jinshan Chemical Reagent Co., Ltd.), sodium dihydrogen phosphate (AR analytical pure, sample purchased from Chengdu Jinshan Chemical Reagent Co., Ltd.), silver nitrate (AR analytical pure, sample purchased

from Sinopharm Chemical Reagent Co., Ltd.), and MB (≥98%, reagent purchased from Solarbio).

**2.2. Preparation of AC.** The AC used in the experiments was prepared from barley straw via a hydrothermal method and subsequent activation. In the first step, barley straw powder was mixed with a citric acid solution at a specific mass fraction, at a mass ratio of 1:10. The hydrothermal temperature was set at 240 °C, and the reaction time was 120 min. The AC was initially impregnated for a designated period and then dried in an oven at 105 °C for 24 h. Subsequently, the AC underwent activation in a tube furnace at a high temperature for 1 h. Different temperature parameters were tested, revealing that the specific surface area of the prepared AC was highest at a temperature of 1100 °C. The AC produced under these specified conditions was used in all subsequent experiments.

**2.3. Preparation of Ag$_3$PO$_4$.** A certain mass of AgNO$_3$ (2.55g) was weighed and dissolved in 90 mL of deionized water to form liquid A. A certain mass of Na$_2$HPO$_4$·12H$_2$O (1.79g) was weighed and dissolved in 30 mL of deionized water to form liquid B. A molar ratio of AgNO$_3$ to Na$_2$HPO$_4$·12H$_2$O of 3:1 was maintained. Solution A was added to solution B dropwise, and the mixed solution was stirred on a magnetic stirrer for 10 min. The resulting sample was dried in an oven at 70 °C for 12 h to obtain Ag$_3$PO$_4$.

**2.4. Preparation of AC/Ag$_3$PO$_4$ Composites.** The preparation process of the composites is depicted in Figure 1. First, silver phosphate dispersions with mass fractions of 1, 2,



**Figure 1.** Flowchart of AC/Ag$_3$PO$_4$ composite preparation.

3, 4, and 5 wt % were prepared. Subsequently, 50 mL of each dispersion was combined with 1 g of AC. To ensure effective contact between the AC and silver phosphate and to prevent silver phosphate precipitation, the composites were subjected to sonication and stirred at 60 °C for 1 h, followed by being

washed three times with ultrapure water and dried for further characterization and performance analysis.

**2.5. Analysis and Experiments.** *2.5.1. Characterization.* The samples were subjected to a series of characterization techniques. Physical adsorption was conducted through the Brunauer−Emmett−Teller (BET) method with an ASAP 2460 instrument. Microscopic morphology was examined using a scanning electron microscope (JSM-IT800 model, JEOL, Japan) operating within a voltage range of 3−30 kV. Elemental species and their relative surface contents were determined using an energy spectrometer integrated with the scanning electron microscope. Scanning electron microscopy (SEM), which was performed on a Quanta 200F electron microscope, was employed to probe the surface morphology. Transmission electron microscopy (TEM) was performed using the FEI Talos F200x G2 model, operating at 200−300 kV. X-ray diffraction (XRD) analysis was conducted using a BRUCKER D8 ADVANCE X-ray diffractometer. X-ray photoelectron spectroscopy (XPS) patterns were acquired and analyzed using the Thermo Scientific Escalab 250Xi XPS instrument. Further characterizations included Raman spectroscopy (Renishaw Raman Horiba spectrometer, laser wavelength 532 nm$^{-1}$), Fourier-transform infrared (FTIR) spectroscopy using a Nicolet Magna 560 E.S.P FTIR spectrometer, and organic elemental analysis performed with an EA Vario MACRO cube instrument. The concentrations of MB were measured using an ultraviolet−visible−near-infrared spectrometer.

*2.5.2. Removal Rate Experiments.* To assess the performance of the composites, we conducted tests on both AC and AC/Ag$_3$PO$_4$ composites. Initially, MB was chosen as the pollutant model. We weighed 1 g of prepared AC and AC/Ag$_3$PO$_4$ and mixed them separately with seven groups of 50 mL MB solutions, each with a concentration of 100 mg/L. These mixtures were then placed in the photocatalytic reaction chamber (Solar-500Q, xenon lamp, Newbie, Beijing, China). We kept all experimental conditions consistent, with the only variation being the type of remover used. Adsorption experiments were meticulously performed under dark conditions. In each assay, 20 mg of the adsorbent was thoroughly mixed with 20 mL of methylene blue solution. The concentration of methylene blue in the supernatant was
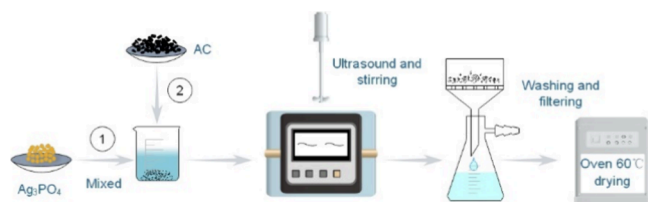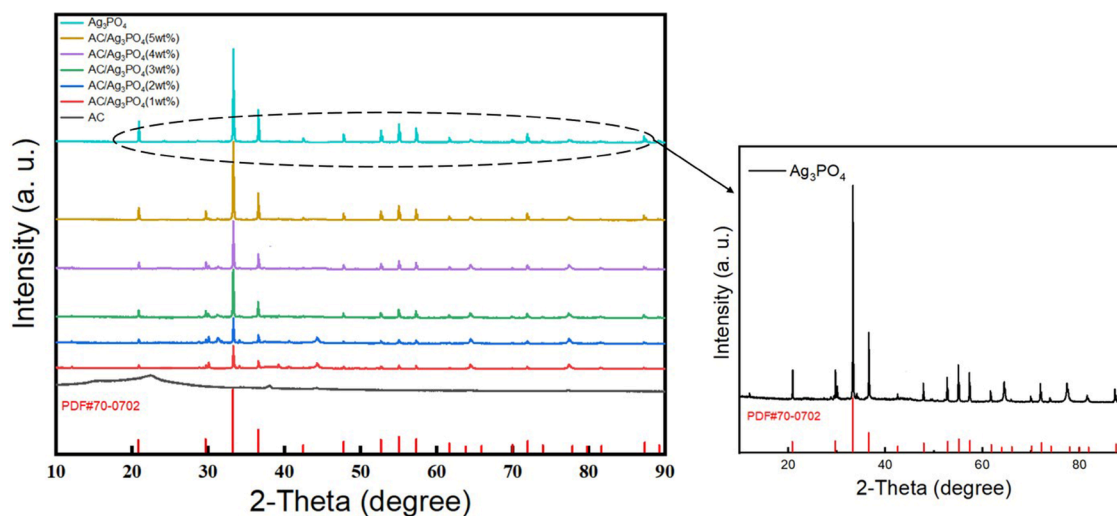


**Figure 2.** X-ray diffraction patterns of AC, Ag$_3$PO$_4$, and AC/Ag$_3$PO$_4$ composites.

**Figure 3.** SEM images of AC/Ag$_3$PO$_4$ composites: (a) AC, (b) AC/Ag$_3$PO$_4$ (1 wt %), (c) AC/Ag$_3$PO$_4$ (2 wt %), (d) AC/Ag$_3$PO$_4$ (3 wt %), (e) AC/Ag$_3$PO$_4$ (4 wt %), (f) AC/Ag$_3$PO$_4$ (5 wt %).
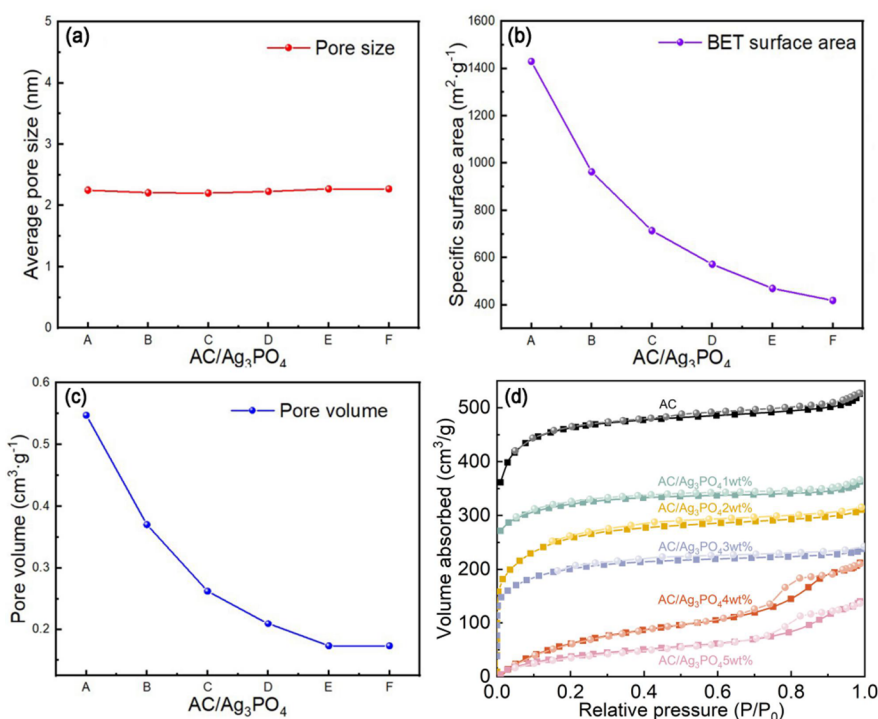


**Figure 4.** Specific surface area of the AC/Ag$_3$PO$_4$ complex: (a) average pore size, (b) specific surface area, (c) pore volume, (d) isotherm model.

accurately determined postcentrifugation, utilizing the intermittent sampling technique for sample collection.

## 3. RESULTS AND DISCUSSION

### 3.1. Structure and Characterization of AC/Ag$_3$PO$_4$.
Silver phosphate exhibits a body-centered cubic lattice, allowing for comprehensive peak normalization of its structure. The XRD patterns of pure AC, Ag$_3$PO$_4$, and the AC/Ag$_3$PO$_4$ composites are shown in Figure 2. The distinct XRD pattern of silver phosphate aligned seamlessly with the powder diffraction file JCPDS #70-0702.[37] Specifically, the angles 20.89°, 29.70°, 33.29°, and 36.59° corresponded to the crystallographic planes denoted as (110), (200), (210), and (211), respectively. The remarkably clear and sharp peaks observed in the XRD profile of silver phosphate confirm its purity and high crystallinity. Notably, under the experimental conditions, the synthesized

silver phosphate showed no extraneous peaks, indicating its lack of impurities. In the field of photocatalysis, high crystallinity of silver phosphate often leads to reduced lattice defects, thereby enhancing its photocatalytic efficiency.[38,39] This characteristic distinguishes the synthesized material as an exemplary photocatalytic agent. Upon the incorporation of silver phosphate, the characteristic peaks of AC began to diminish, while those of silver phosphate progressively intensified.

Figure 3 presents the scanning electron microscopy (SEM) images of the AC/Ag$_3$PO$_4$ composites. SEM analysis shows AC/Ag$_3$PO$_4$ composites preserving AC's porous structure, despite Ag$_3$PO$_4$ integration. Silver phosphate, synthesized utilizing Na$_3$H$_2$PO$_4$·12H$_2$O and AgNO$_3$, exhibited a distinctive rhombic dodecahedral morphology.[40] The photocatalytic ability of silver phosphate is related to its morphological

attributes. Specifically, the rhombic dodecahedral form enhanced the photocatalytic potential of silver phosphate. Furthermore, a close examination of the composite's SEM images suggests that silver phosphate tended to occupy the pore interstices within the AC. This juxtaposition of the dodecahedral structure of silver phosphate within the pore cavities of the AC is illustrated in Figure 3a,e. However, a deeper analysis of the SEM data revealed that as the concentration of silver phosphate increased, gradual $Ag_3PO_4$ accumulation occurred within the AC's pore cavities. The observed accumulation of silver phosphate not only impedes the pore entrances, leading to a reduction in the specific surface area of the AC, but also induces notable alterations in its surface physical properties. This phenomenon has been substantiated by XRD and SEM analyses. As the concentration of silver phosphate increases, its distinctive peaks in the XRD patterns become increasingly pronounced, indicative of its growing presence. Concurrently, SEM imaging reveals the gradual buildup of silver phosphate within the pores of the activated carbon, culminating in marked changes to its surface physical attributes. These findings have been further validated by BET studies, which corroborate the impact on the surface area and porosity of the AC. These changes indicate a decrease in the AC sorptive capacity, which in turn affected the composite's ability to efficiently sequester pollutants. A comprehensive exploration of the optimal compositional conditions necessitates a holistic assessment through subsequent characterization and multifaceted evaluations.

In Figure 4, labels A through F on the horizontal axis represent the following adsorbents: AC, AC/$Ag_3PO_4$ (1 wt %), AC/$Ag_3PO_4$ (2 wt %), AC/$Ag_3PO_4$ (3 wt %), AC/$Ag_3PO_4$ (4 wt %), and AC/$Ag_3PO_4$ (5 wt %). To elucidate the effects of varying silver phosphate composite concentrations on the porous structure of the AC, several metrics, including pore diameter, specific surface area, and pore volume, were characterized using physical adsorption techniques. The specific surface area, alongside the average pore size and pore volume, were determined utilizing the multilayer adsorption model (BET model) and the Barrett–Joyner–Halenda (BJH) method, respectively. The corresponding results are illustrated in Figure 4 and Table 1. The initial

**Table 1. Material's Specific Surface Area, Pore Diameter, and Porosity**

| sample | $S_{BET}$ (m²/g) | $D_P$ (nm) | $P$ (%) |
|---|---|---|---|
| AC | 1429.59 | 0.23 | 0.55 |
| AC/$Ag_3PO_4$ (1 wt %) | 962.97 | 0.23 | 0.37 |
| AC/$Ag_3PO_4$ (2 wt %) | 723.62 | 0.23 | 0.26 |
| AC/$Ag_3PO_4$ (3 wt %) | 572.04 | 0.23 | 0.21 |
| AC/$Ag_3PO_4$ (4 wt %) | 469.87 | 0.23 | 0.17 |
| AC/$Ag_3PO_4$ (5 wt %) | 423.39 | 0.23 | 0.17 |

specific surface area of the AC was 1429.59 m²/g. However, as the mass fraction of the incorporated silver phosphate increased, the specific surface area decreased, reaching values of 962.97 (1 wt %), 723.62 (2 wt %), 572.04 (3 wt %), 469.87 (4 wt %), and 423.39 (5 wt %) m²/g. Notably, the specific surface area of the AC/$Ag_3PO_4$ composites was significantly lower than that of pristine AC. When the silver phosphate concentration reached 5 wt %, the specific surface area decreased to 423.39 m²/g, approximately one-third of its original value. This reduction is attributable to an excess of

silver phosphate covering the AC's surface, leading to partial pore blockage. Such a reduced specific surface area may compromise the composite's adsorption efficiency.[41−43] This deduction, depicted in Figure 4b,c, aligns with the SEM results. Figure 4a highlights that the silver phosphate concentration had a negligible impact on the AC average pore size, which remained stable at ∼2.3 nm. As the silver phosphate concentration increased, both the mean pore volume (Figure 4c) and the specific surface area (Figure 4b) consistently decreased, reaching values of 0.37 (0 wt %), 0.26 (1 wt %), 0.21 (2 wt %), 0.17 (3 wt %), 0.17 (4 wt %), and 0.17 (5 wt %) cm³/g. In the context of pollutant sequestration, the pore volume primarily facilitates the mobility of adsorbates on the AC surface, thereby enhancing the adsorption capacity of the AC.

Figure 5 presents the TEM micrographs of silver phosphate. The high-resolution TEM (HR-TEM) image of silver phosphate (Figure 5b) revealed lattice fringes with spacings of 0.242 and 0.245 nm, where the angle between the two measured layers was ∼70°. These spacings corresponded to the (211) and ($2\bar{1}\bar{1}$) planes of silver phosphate, in accordance with the JCPDS #70-0702 database. The spacings and angles further support the XRD patterns of $Ag_3PO_4$ (Figure 2). The distinct lattice fringes confirm that the synthesized silver phosphate exhibited a monocrystalline structure. This assertion is corroborated by the selected-area electron diffraction (SAED) pattern (Figure 5c). Furthermore, the Energy Dispersive X-ray Spectroscopy (EDS) results, depicted in Figure 5d−g, demonstrate a homogeneous distribution of the constituent elements—Ag, O, and P. This evidence, in conjunction with the X-ray Diffraction (XRD) patterns presented in Figure 1, strongly indicates the efficient synthesis of silver phosphate.

The crystalline structure of the AC/$Ag_3PO_4$ composite was examined via field-emission TEM. The HR-TEM image (Figure 6b) revealed a granular nanostructure of silver phosphate dispersed within the AC matrix. A lattice spacing of 0.245 nm, corresponding to the (211) plane of silver phosphate, was observed. This observation aligns with the data from the XRD analysis and the representation in Figure 5b. The SAED patterns (Figure 6c) exhibited two distinct rings: (110) and (100).[44,45] These patterns are consistent with the interlayer spacings of the graphite plane, as supported by reference data (JCPDS #41-1487), confirming the coexistence of both components AC and $Ag_3PO_4$ in the composite. Furthermore, EDS mapping (Figure 6d−h) revealed a visual representation of the elemental distributions of C, Ag, O, and P within the samples. Overall, these results strongly confirm the composition of the synthesized AC/$Ag_3PO_4$ composite as a combination of a graphite-like carbon framework and $Ag_3PO_4$.

The FTIR spectrum in Figure 7a highlights a peak at 3418 cm⁻¹, tied to AC's -NH₂ vibrations. This attribution is supported by Figure 7b, which shows that thermally activated AC exhibits a peak at 3418 cm⁻¹. However, it is critical to note the pronounced breadth of this band in Figure 7a. Consequently, the broad band manifesting near 3500 cm⁻¹ encompasses the peak at 3418 cm⁻¹. Predominantly, the peak in the vicinity of 3500 cm⁻¹ is synonymous with the O−H stretching vibrations, a hallmark of adsorbed water molecules. This observation intimates that the spectral feature at 3418 cm⁻¹ might not be exclusively attributable to the -NH₂ functional group; rather, the influence of adsorbed water could be significantly contributory. The considerable width
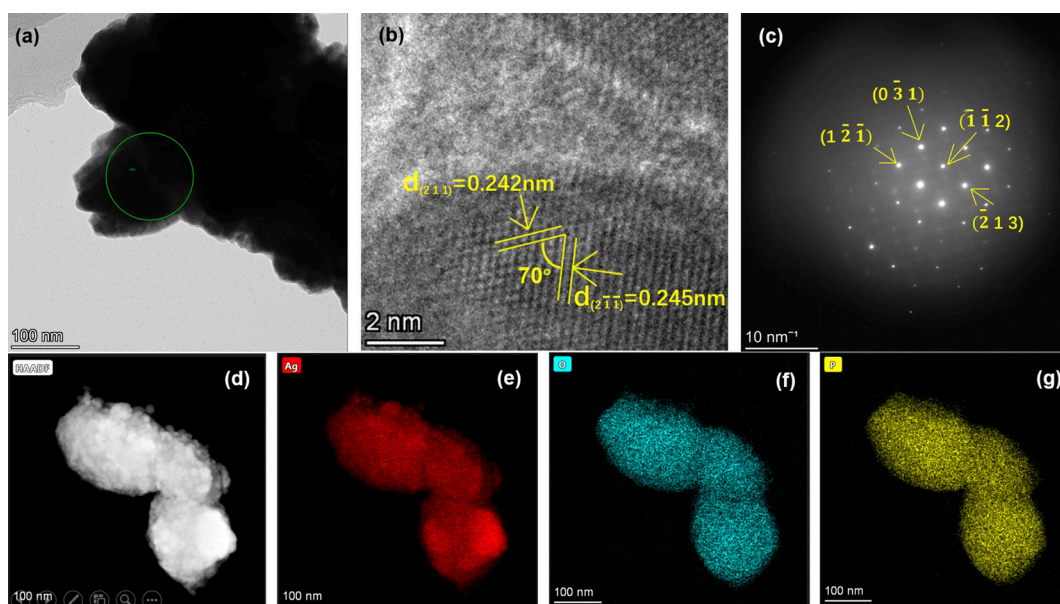
**Figure 5.** TEM images of silver phosphate: (a) TEM image, (b) high-resolution TEM image, (c) SAED pattern, (d) HAADF image, and (e−g) mapping of (e) Ag element, (f) O element, and (g) P element.
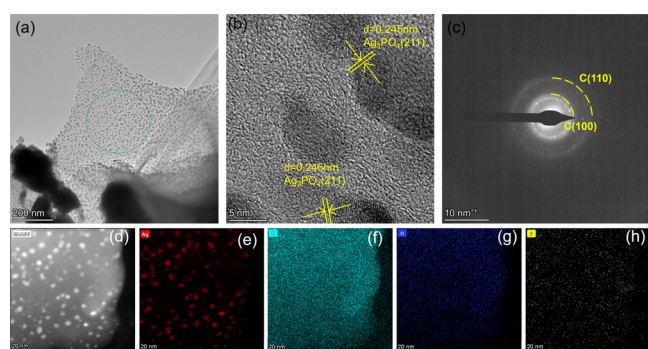


**Figure 6.** TEM images of the AC/Ag$_3$PO$_4$ composite: (a) TEM image, (b) high-resolution TEM image, (c) SAED pattern, (d) HAADF image, and (e−h) mapping of (e) Ag element, (f) C element, (g) O element, and (h) P element.

and intensity of this band suggest extensive interactions between water molecules and the composite surface. This could be a result of either the inherent hydrophilicity or environmental hygroscopicity of the material. Such an

interpretation aligns with the frequent occurrence of water adsorption in porous materials, including activated carbon. The peak at 1650 cm$^{-1}$ corresponded to the C=C skeletal vibration, which affects infrared transmittance. The characteristic absorption peak at 1400 cm$^{-1}$ can be attributed to the combined bending and stretching vibrations induced by water molecules adsorbed onto the Ag$_3$PO$_4$ surface and hydroxyl groups. These hydroxyl groups can interact with photogenerated holes, leading to the generation of strong oxidizing radicals, thereby enhancing the photocatalytic degradation capabilities of Ag$_3$PO$_4$ toward MB. Furthermore, the P=O vibrational peak, observed at 1007 cm$^{-1}$ and associated with the PO$_4^{3-}$ group, suggests a strong interaction between AC and silver phosphate, indicating their successful integration. In the low-frequency range, the absorption peak at 510 cm$^{-1}$ corresponds to the presence of the C−H bond, indicating the combination of the carbon backbone with trace amounts of H ions found in AC. As the mass fraction of the silver phosphate composite increased, the absorption peaks on the FTIR spectrum intensified, overshadowing the original AC infrared peaks. This indicates an enhanced affinity between AC and silver phosphate in the composites. These results, in
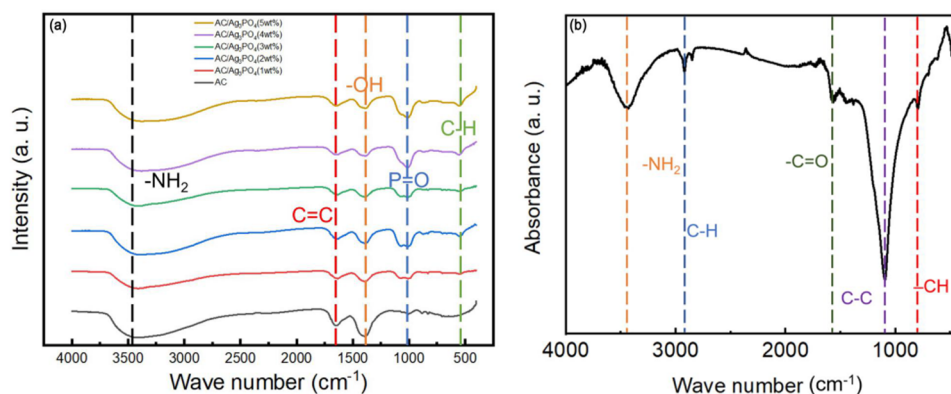


**Figure 7.** FTIR spectra of AC/Ag$_3$PO$_4$ composites (a) and AC (b).

combination with the SEM (Figure 3) and TEM (Figure 6) images, confirm that the composites were successfully fabricated.

Raman spectroscopy (Figure 8) verifies the AC/Ag$_3$PO$_4$ composites' graphitic structure. This observation is consistent
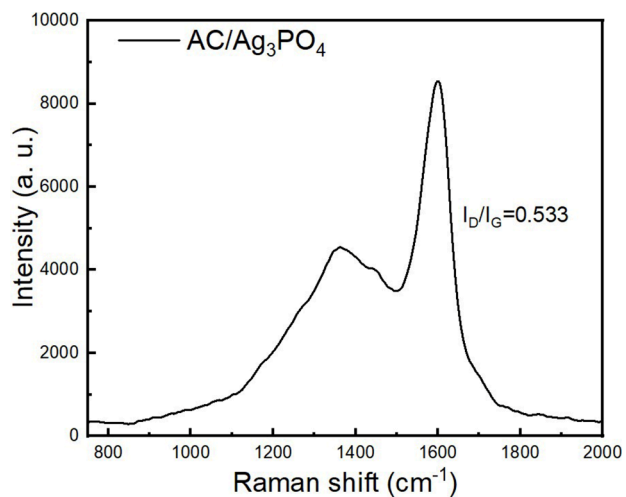


**Figure 8.** Raman spectrum of the AC/Ag$_3$PO$_4$ (3 wt %) composite.

with the XRD results (Figure 2). The Raman spectra of the AC/Ag$_3$PO$_4$ composites exhibited a D-band peak at 1371 cm$^{-1}$ and a G-band peak near 1601 cm$^{-1}$. The ratio between these peaks ($I_D/I_G$) was 0.533. The $I_D/I_G$ ratio, a crucial parameter in Raman spectroscopy, is derived by comparing the intensities of the D-band and the G-band. These bands correspond, respectively, to the degree of defects (disorder) and graphitization within the material. A diminished ratio signifies a relatively lower intensity of the D-band, which is indicative of defects, in comparison to the G-band that reflects graphitization. Consequently, a reduced $I_D/I_G$ ratio is emblematic of a

material harboring fewer imperfections and aligning more closely with the ideal graphite structure, thereby denoting elevated purity and enhanced structural stability. The $I_D/I_G$ ratio for the pristine activated carbon (AC) was determined to be 1.24. This ratio indicates a structure akin to graphite, reflecting a balance between the presence of graphitic domains and disordered carbon structures within the AC. In the context of AC/Ag$_3$PO$_4$ composites, a lower $I_D/I_G$ ratio suggests that the activated carbon component within the composite retains a substantial degree of graphitization while manifesting a minimized extent of defects, which is pivotal for its overall performance.[46] A lower ratio indicates greater purity and a more stable structure of the AC. Furthermore, higher graphitization promoted enhanced electron transport on the AC surface, thereby enhancing the photocatalytic efficiency of the composites.

Figure 9 illustrates the X-ray photoelectron spectra of the AC/Ag$_3$PO$_4$ composites. Figure 9a provides a comprehensive elemental mapping, revealing the presence of four elements: Ag, P, O, and C. Analytical insights reveal that the binding energies of Ag 3d (Figure 9b) were 368.12 and 374.14 eV, corresponding to the spin−orbit splitting peaks of Ag 3d$_{5/2}$ and Ag 3d$_{3/2}$,[47,48] respectively. These values indicate the +1 valence state of the Ag element in the composite. Figure 9c depicts peaks associated with the C−C skeleton of AC and the presence of C−O and C=O functional groups, corresponding to 284.8, 287.16, and 288.89, respectively. This, coupled with the FTIR analysis results from Figure 6, suggests successful composite preparation. The O 1s peak in Figure 9d at 530.68 eV and the P 2p peak in Figure 9e at 132.63 eV are attributable to P$^{5+}$ and O$^{2-}$ in Ag$_3$PO$_4$,[49] while 532.60 is the peak for surface adsorbed O. The XPS findings are consistent with the FTIR, SEM, and TEM results, further confirming the successful fabrication of the composites.

The AC/Ag$_3$PO$_4$ composites' effectiveness against MB, a representative contaminant, was assessed using a photo-
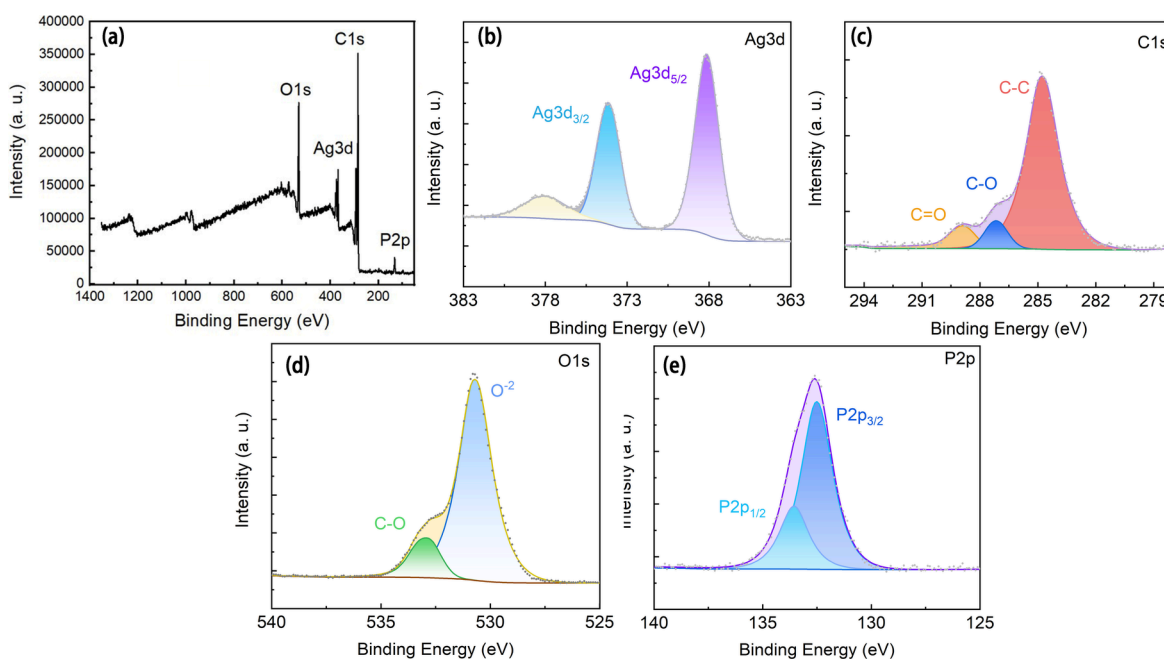


**Figure 9.** XPS spectra of the AC/Ag$_3$PO$_4$ (3 wt %) composite: (a) full spectrum, (b) Ag spectrum, (c) C spectrum, (d) O spectrum, (e) P spectrum.
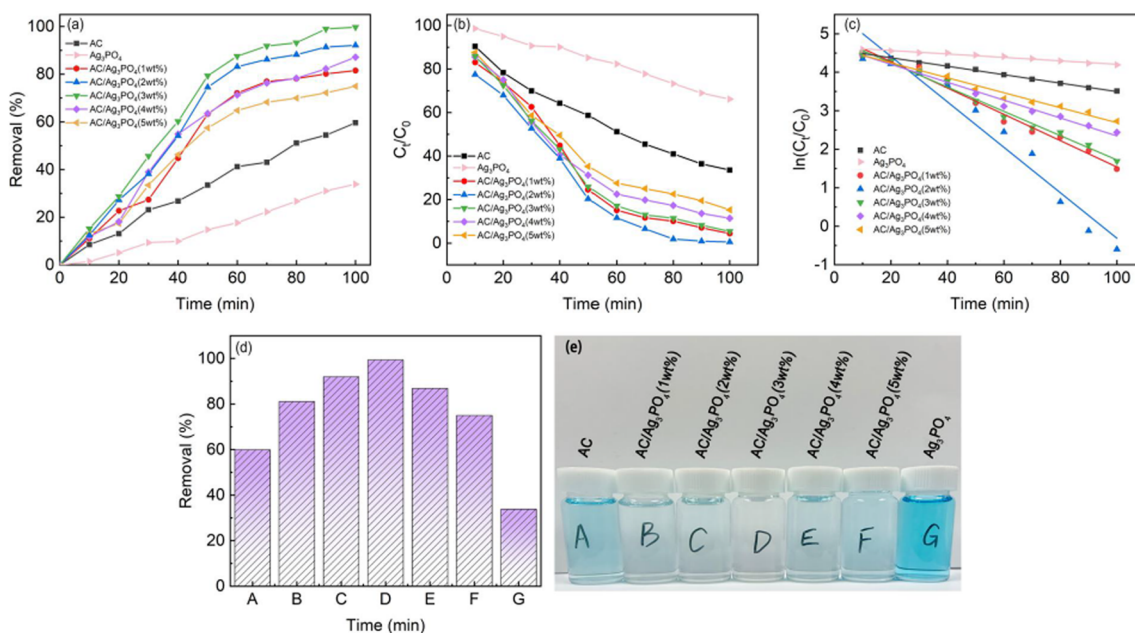
**Figure 10.** MB removal efficiencies of AC, $Ag_3PO_4$, and $AC/Ag_3PO_4$ composites: (a) removal efficiency curves, (b) concentration ratios ($C_t/C_0$), (c) kinetics plots, (d) bar chart of removal efficiencies, (e) residual MB image after illumination.

catalytic reactor. Periodic sampling was conducted, and the results are presented in Figure 10. The data in Figure 10a,d reveal that the contaminant removal efficiencies for the seven sample sets within 100 min were 59.9, 81.1, 92, 99.4, 86.9, 75.0, and 33.8%. Labels A to G in Figure 10d,e represent AC, $AC/Ag_3PO_4$ (1 wt %), $AC/Ag_3PO_4$ (2 wt %), $AC/Ag_3PO_4$ (3 wt %), $AC/Ag_3PO_4$ (4 wt %), $AC/Ag_3PO_4$ (5 wt %), and $Ag_3PO_4$. The removal efficiency exhibited a time-dependent increase, and the composites demonstrated superior MB removal capabilities to standalone AC under identical conditions. As the concentration of MB decreased in the solution, the removal rate plateaued. This is attributed to the reducing concentration, which reduced comprehensive inter-action with active sites, thereby affecting adsorption and photocatalysis.[50,51] Figure 10d indicates that a silver phosphate concentration of 3 wt % yielded the highest removal rate. Surpassing this concentration resulted in declining rates. The XRD results revealed that the optimal uniform distribution of silver phosphate on the AC was 5 wt %, theoretically offering peak photocatalytic effects. However, empirical evaluations revealed that the highest removal rate occurred at 3 wt % and not 5 wt %. This anomaly arises from the cyclic mechanism of adsorption−photocatalysis−adsorption inherent in the com-posite, accentuated by the presence of AC. Photocatalysis primarily occurs on the catalyst's surface. An excessive concentration of silver phosphate in the composite reduces its light transmittance, limiting its ability to generate the necessary hydroxyl and reactive oxygen species, thereby reducing photocatalytic efficiency. Increasing the amount of silver phosphate within the composite reduces the specific surface area of AC, resulting in some adsorption sites being occupied and, thus, reducing its adsorptive capacity. This compromises the interaction between silver phosphate and MB, leading to a decrease in photocatalytic efficacy. MB molecules, after being adsorbed onto the composite's surface through AC, participate in direct photocatalysis with silver phosphate, ultimately degrading into $CO_2$ and $H_2O$. As these

molecules degrade, fresh adsorption sites become available, continuing the cycle.

Figure 10c illustrates the kinetic profiles associated with the adsorption and degradation processes of AC and silver phosphate. The reaction rate constants ($k$) for the seven different material sets were determined to be 0.0110, 0.0346, 0.0581, 0.0318, 0.0231, 0.0195, and 0.0045 $min^{-1}$ (Table 2).

**Table 2. Comparison of the Rate Constants $k$ at the First Level of the Composites**

| sample | $k$ ($min^{-1}$) | $R^2$ |
|---|---|---|
| AC | 0.0110 | 0.9976 |
| $AC/Ag_3PO_4$ (1 wt %) | 0.0346 | 0.9816 |
| $AC/Ag_3PO_4$ (2 wt %) | 0.0581 | 0.9562 |
| $AC/Ag_3PO_4$ (3 wt %) | 0.0318 | 0.9882 |
| $AC/Ag_3PO_4$ (4 wt %) | 0.0231 | 0.9855 |
| $AC/Ag_3PO_4$ (5 wt %) | 0.0195 | 0.9832 |
| $Ag_3PO_4$ | 0.0045 | 0.9808 |

The composite with 2 wt % silver phosphate exhibited enhanced reaction kinetics, showing a 5.27 times higher reaction rate compared with pristine AC and 12.91 times higher reaction rate compared to $Ag_3PO_4$. The degradation rate profile of silver phosphate indicates a diminished efficacy in rapidly removing methylene blue at elevated concentrations. This reduction in performance can be ascribed to the decreased light transmittance of the solution when the methylene blue content is excessively high.[32,33] The con-sequent decline in available light critically impacts the photocatalytic efficiency. Furthermore, at such high concen-trations, the active sites on the silver phosphate surface are likely to be rapidly occupied by the dye molecules, leading to saturation. This saturation of active sites contributes to the deceleration of the degradation process. The interplay between reduced light penetration and site saturation underscores the challenges in photocatalytic degradation under conditions of high dye concentration. The composite overcomes silver

phosphate's limitations in degrading high-concentration pollutants through AC's superior adsorption. This synergistic combination leverages the robust adsorptive properties of activated carbon, thereby enhancing the overall efficacy of the composite in tackling pollutants at higher concentrations. To quantitatively assess the pollutant removal efficiency across various composites, the photodecomposition dynamics can be approximated by the relation $-\ln(C_t/C_0) = kt$. Here, $t$ represents the reaction duration, $C_0$ denotes the initial concentration of the reactants, $C_t$ represents the concentration of the reactants at a given time $t$, and $k$ represents the reaction rate constant (expressed in $\text{min}^{-1}$). The relationship between $\ln(C_t/C_0)$ and time $t$ for the seven reactant groups exhibited strong linearity, consistent with the kinetics of the primary reaction.

In summary, although AC demonstrates a certain efficiency in removing MB from water, its adsorption removal effectiveness is relatively limited. Data from Figure 10 indicates that within 100 min, the removal rate of MB by pure AC only reached 59.9%, primarily due to the lack of photocatalytic functionality in AC itself. Thus, the removal of MB relies heavily on adsorption, constraining its capacity for rapid MB elimination. Similarly, the removal rate by $Ag_3PO_4$ alone is only 33.8%, suggesting that solitary photocatalytic capability also limits the rapid removal of MB. Kinetic analysis through reaction rate constant fitting revealed that, while the reaction rate constant for AC ($0.0110\ \text{min}^{-1}$) surpasses that of $Ag_3PO_4$ used alone ($0.0045\ \text{min}^{-1}$), it falls significantly short of the $0.0581\ \text{min}^{-1}$ achieved by the $AC/Ag_3PO_4$ (2 wt %) composite. This underscores the limitations of relying solely on adsorption or photocatalysis for MB removal from aqueous solutions. Compared to using AC or $Ag_3PO_4$ individually, the $AC/Ag_3PO_4$ composite material significantly enhances MB removal efficiency by integrating both adsorption and photocatalysis mechanisms, thereby highlighting its superiority in water treatment applications. The observation that the rate constant of composites with 2% $Ag_3PO_4$ is significantly higher than that of composites containing 3% $Ag_3PO_4$, while the peak removal rate is achieved at 3 wt %, suggests an intriguing interplay between photocatalytic activity and adsorption capacity. This disparity might be ascribed to the fact that a 3 wt % $Ag_3PO_4$ concentration strikes an optimal balance, enhancing photocatalytic activity while preserving robust adsorption capabilities. Conversely, the 2% $Ag_3PO_4$ composite, despite exhibiting a higher rate constant, could potentially underperform in terms of the synergistic impact of photocatalytic activity and adsorption capacity. Such a configuration accentuates the efficiency of an adsorption−photocatalytic cycling system, revealing a nuanced dependency of photocatalytic efficiency on the specific concentration of $Ag_3PO_4$ in the composite.

To elucidate the mechanism underlying methylene blue degradation by the $AC/Ag_3PO_4$ composites, experimental and computational analyses of their adsorption properties were conducted. As depicted in Figure 11a,b, the equilibrium adsorption capacities of AC and varying $Ag_3PO_4$ loadings (1, 2, 3, 4, and 5 wt %) were observed to be 479.44, 406.36, 360.37, 319.47, 284.73, and 246.45 mg/g, respectively. A decline in adsorption capacity with increasing $Ag_3PO_4$ loading was noted, likely due to $Ag_3PO_4$ occupying AC's active adsorption sites, a conclusion supported by BET and SEM analysis. It is noteworthy that all composites reached adsorption equilibrium at 180 min after rapid adsorption in the early stage, showing a
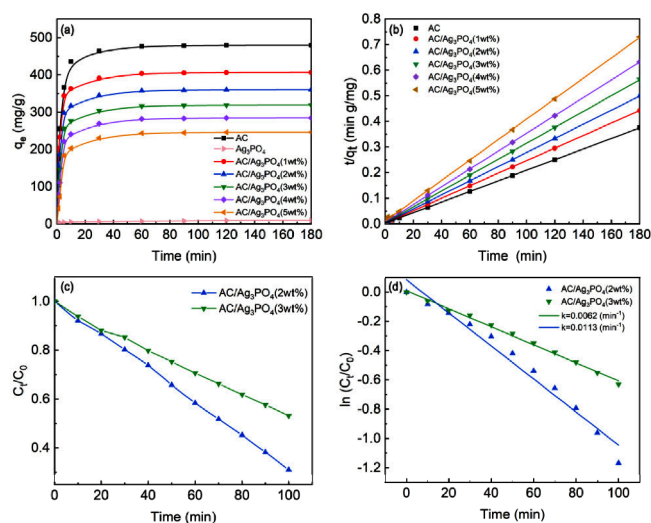


**Figure 11.** Adsorption analysis for AC, $Ag_3PO_4$, and $AC/Ag_3PO_4$ composites: (a) equilibrium adsorption profiles, (b) proposed secondary kinetics models, and (c) concentration ratios ($C_t/C_0$) and (d) corresponding kinetic plots for the photocatalytic activity of $AC/Ag_3PO_4$ (2, 3 wt %).

similar adsorption trend to that of pure AC. Fitting analysis indicated a better alignment with the secondary kinetic model over the primary kinetic model, as evidenced by $R^2$ values exceeding 0.9999, suggesting a predominance of chemisorption in the adsorption process.

The study subsequently compared the photocatalytic performance of composites containing 2 and 3 wt % silver phosphate. Given their superior adsorption capabilities, a 200 mg/L methylene blue solution was used. For each test, 20 mg of the catalyst was combined with 50 mL of MB solution and allowed to adsorb in a dark environment for 180 min to achieve equilibrium. Postadsorption, the samples underwent photocatalytic processing. As depicted in Figure 11c,d, the 2 wt % $Ag_3PO_4$ composites demonstrated higher reaction kinetics than the 3 wt % variant, aligning with the analysis presented in Figure 10. This highlights the nuanced dependency of photocatalytic efficiency on the specific $Ag_3PO_4$ concentration in the composites. AC, serving as a support carrier within composites, significantly enhanced performance.[29] Its robust adsorption properties effectively concentrated dye molecules near photocatalytic sites, shortening the light response time and increasing the interaction area with contaminants. Furthermore, AC's high adsorption capacity reduced the concentration of methylene blue in solution, thereby improving light transmittance and creating optimal photocatalytic conditions for $Ag_3PO_4$. Consequently, the $AC/Ag_3PO_4$ composites exhibit superior photocatalytic efficiency.

**3.2. Evaluation and Analysis of the Cycle Stability of $AC/Ag_3PO_4$ Composites.** Figure 12 provides a detailed examination of the cyclic stability of the $AC/Ag_3PO_4$ composite. Regeneration of $AC/Ag_3PO_4$ composites includes hydrochloric acid soaking, thorough rinsing, and drying at 60 °C, restoring their adsorptive capacity. After drying, these composites are ready for reuse in subsequent experiments. This approach ensures effective removal of adsorbed substances and restoration of the composites' adsorptive properties. Cyclic regeneration studies were conducted via adsorption−desorption experiments. The accompanying illustration depicts the cyclical adsorptive behavior of MB by the $AC/Ag_3PO_4$
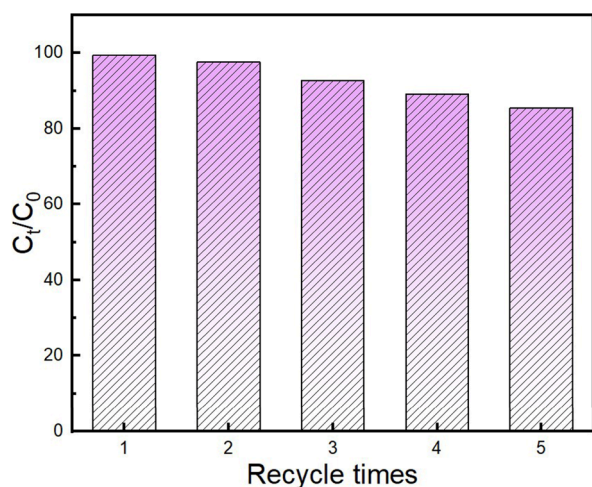
**Figure 12.** Effect of the number of regeneration cycles of AC/Ag$_3$PO$_4$ (3 wt %) on MB adsorption.



**Figure 14.** MB removal mechanism of the AC/Ag$_3$PO$_4$ composite.

composites. Cycling tests, conducted under specific conditions (100 mg/L MB, pH 7, 100 min, 308 K), show the composite maintaining high MB removal efficiency across five cycles. As indicated by the graphical representation, the MB removal efficiencies over five consecutive cycles were 99.4, 97.6, 92.8, 89.1, and 85.5%. The composite retained a high removal efficiency even after five cycles, confirming its resilience as an adsorptive–photocatalytic material.

After desorption of the cycled AC/Ag$_3$PO$_4$ (3 wt %) composites, the composites were characterized via FTIR spectroscopy (Figure 13). The absorption maxima observed
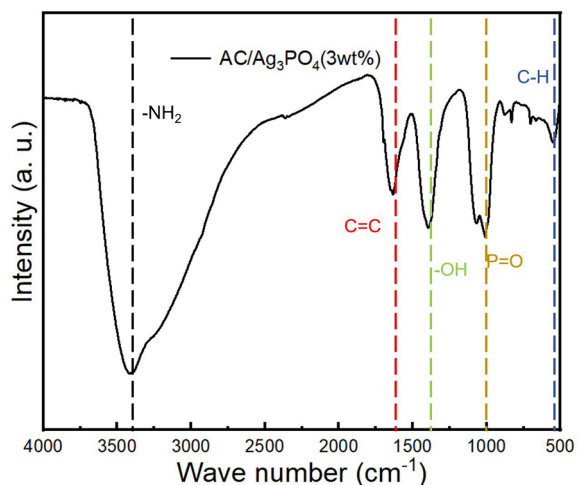


**Figure 13.** Infrared absorption spectrum of the AC/Ag$_3$PO$_4$ (3 wt %) sample after recycling.

in the spectral representation align with those in Figure 7, indicating minimal perturbations in the chemical bonds of the composite after five iterative cycles. In conjunction with the cycling performance insights from Figure 11, the characterization results substantiate the composite's robustness and effectiveness as an efficient contaminant removal agent.

As depicted in Figure 14, MB was initially adsorbed by the AC, effectively increasing the contact area between the dye molecules and the photocatalyst, thereby reducing the response time. Once exposed to light, the adsorbed MB molecules were degraded into CO$_2$ and H$_2$O. The architecture
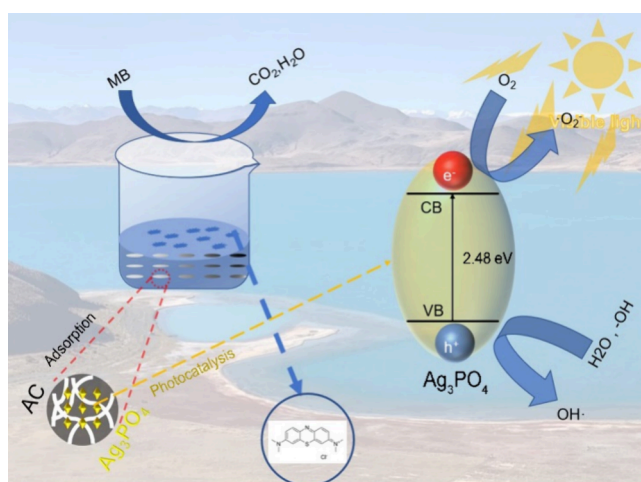
of AC provided ample space for the decomposition of the adsorbed MB by Ag$_3$PO$_4$, significantly expediting both the adsorption and subsequent decomposition of MB. This created vacancies for MB molecules outside the composite, promoting the attraction and uptake of new MB molecules. Consequently, a synergistic "adsorption–photodegradation" process evolved, leading to an overall pollutant removal efficiency that substantially surpassed those of conventional absorbents and photocatalysts.

## 4. CONCLUSIONS

In this study, biomass-derived AC was proficiently fabricated via hydrothermal carbonization coupled with alkaline activation techniques. The silver phosphate was ultrasonically loaded onto the AC. Comprehensive characterization assessments validated the synthesis of this composite. Trials on MB removal revealed the composite's exceptional adsorptive and photocatalytic capacity at a Ag$_3$PO$_4$ concentration of 3 wt %. At this concentration, the composite achieved 99.4% MB removal within 100 min. Moreover, the reaction rate of the composite was 2.89 times that of standalone AC. Over five consecutive cycles, the composite exhibited MB removal efficiencies of 99.4, 97.6, 92.8, 89.1, and 85.5%, thereby demonstrating high stability. Challenges associated with secondary contamination, a consequence of AC's exhaustion and desorption, were addressed while enhancing its performance. The introduction of silver phosphate as a photocatalyst onto the AC resulted in an adsorption–photocatalysis–adsorption cycle, effectively circumventing issues of adsorbent desorption and the accompanying secondary pollution inherent in conventional adsorptive water treatment modalities. Moreover, the research revealed that the MB removal capacity of the composite exceeded that of the standalone AC. The highest pollutant removal efficiency was realized at a silver phosphate concentration of 3 wt %, indicating that this concentration was optimal for the interplay between adsorption and photocatalysis within the framework of pollutant removal. The proposed method involves an adsorption–photocatalysis–adsorption cycle and does not result in secondary pollution. As such, this investigation pioneers a revitalized approach to water pollution treatment.

# ■ AUTHOR INFORMATION

## Corresponding Authors

**Shifeng Wang** — *Key Laboratory of Plateau Oxygen and Living Environment of Tibet Autonomous Region, College of Science, Tibet University, Lhasa 850000, P. R. China; Fujian Quanzhou Peninsula Materials Co., Ltd., Quanzhou 362000, China; Aimoli (Hebei) Technology Co., Ltd, Shijiazhuang 050000, China;* ⊙ orcid.org/0000-0001-6169-2598; Email: wsf@utibet.edu.cn

**Chun Du** — *Key Laboratory of Plateau Oxygen and Living Environment of Tibet Autonomous Region, College of Science, Tibet University, Lhasa 850000, P. R. China;* Email: duchun@utibet.edu.cn

## Authors

**Yihang Yue** — *Key Laboratory of Plateau Oxygen and Living Environment of Tibet Autonomous Region, College of Science, Tibet University, Lhasa 850000, P. R. China*

**Lin Han** — *Key Laboratory of Plateau Oxygen and Living Environment of Tibet Autonomous Region, College of Science, Tibet University, Lhasa 850000, P. R. China;* ⊙ orcid.org/0009-0004-8282-6566

**Bo Ding** — *College of Information Engineering, Xizang Minzu University, Xianyang 712000, China*

**Yanxi Yang** — *Key Laboratory of Plateau Oxygen and Living Environment of Tibet Autonomous Region, College of Science, Tibet University, Lhasa 850000, P. R. China*

**Xiaoju Yue** — *Key Laboratory of Plateau Oxygen and Living Environment of Tibet Autonomous Region, College of Science, Tibet University, Lhasa 850000, P. R. China*

**Qingguo Song** — *Aimoli (Hebei) Technology Co., Ltd, Shijiazhuang 050000, China*

Complete contact information is available at:
https://pubs.acs.org/10.1021/acsomega.4c01011

## Author Contributions

#Y.Y., L.H., and B.D. contributed equally to the work and are considered joint first authors. Conceptualization, Y.Y., L.H. and S.W.; methodology, Y.Y. and B.D.; formal analysis, L.H. and B.D.; investigation, Y.X.Y. and J.Y.; data curation, Y.Y. and L.H.; writing—original draft preparation, Y.Y. and L.H.; writing—review and editing, B.D., S.W., and C.D.; supervision, S.W. and C.D.; project administration, S.W.; funding acquisition, S.W and C.D. Resources, B.D. and Q.S. All authors have read and agreed to the published version of the manuscript.

## Notes

The authors declare no competing financial interest.

# ■ ACKNOWLEDGMENTS

# ■ REFERENCES

(1) Sun, P.; Zhou, S.; Yang, Y.; Liu, S.; Cao, Q.; Wang, Y.; Wågberg, T.; Hu, G. Artificial chloroplast-like phosphotungstic acid — iron oxide microbox heterojunctions penetrated by carbon nanotubes for solar photocatalytic degradation of tetracycline antibiotics in waste-water. *Advanced Composites and Hybrid Materials* **2022**, *5* (4), 3158−3175.

(2) Li, H.; Huang, W.; Qiu, B.; Thabet, H. K.; Alhashmialameer, D.; Huang, M.; Guo, Z. Effective removal of proteins and polysaccharides from biotreated wastewater by polyaniline composites. *Advanced Composites and Hybrid Materials* **2022**, *5* (3), 1888−1898.

(3) Li, Z.; Xie, W.; Yao, F.; Du, A.; Wang, Q.; Guo, Z.; Gu, H. Comprehensive electrocatalytic degradation of tetracycline in waste-water by electrospun perovskite Manganite nanoparticles supported on carbon nanofibers. *Advanced Composites and Hybrid Materials* **2022**, *5* (3), 2092−2105.

(4) Zhu, X.; Wang, Z.; Ren, J.; AlMasoud, N.; El-Bahy, Z. M.; S.Alomar, T.; Zhang, C.; Zhang, J.; Zhou, J.; Li, M.; Wang, D.; Seok, I.; Guo, X. Graphene/polyacrylamide interpenetrating structure hydrogels for wastewater treatment. *Advanced Composites and Hybrid Materials* **2023**, *6* (5), 169.

(5) Naeini, A. H.; Kalaee, M. R.; Moradi, O.; Khajavi, R.; Abdouss, M. Synthesis, characterization and application of Carboxylmethyl cellulose, Guar gam, and Graphene oxide as novel composite adsorbents for removal of malachite green from aqueous solution. *Advanced Composites and Hybrid Materials* **2022**, *5* (1), 335−349.

(6) Wang, B.; Kuang, Y.; Li, M.; Wang, X.; Zhang, X.; Rao, Q.; Yuan, B.; Yang, S. Magnetic surface molecularly imprinted polymers for efficient selective recognition and targeted separation of daidzein. *Advanced Composites and Hybrid Materials* **2023**, *6* (6), 196.

(7) Zhou, Z.; Wu, X.; Lin, Z.; Pang, S.; Mishra, S.; Chen, S. Biodegradation of fipronil: current state of mechanisms of biodegradation and future perspectives. *Appl. Microbiol. Biotechnol.* **2021**, *105* (20), 7695−7708.

(8) Zhou, L.; Yu, Q.; Cui, Y.; Xie, F.; Li, W.; Li, Y.; Chen, M. Adsorption properties of activated carbon from reed with a high adsorption capacity. *Ecological Engineering* **2017**, *102*, 443−450.

(9) Zhang, F.; Lian, M.; Alhadhrami, A.; Huang, M.; Li, B.; Mersal, G. A. M.; Ibrahim, M. M.; Xu, M. Laccase immobilized on functionalized cellulose nanofiber/alginate composite hydrogel for efficient bisphenol A degradation from polluted water. *Advanced Composites and Hybrid Materials* **2022**, *5* (3), 1852−1864.

(10) Ikhlaq, A.; Kasprzyk-Hordern, B. Catalytic ozonation of chlorinated VOCs on ZSM-5 zeolites and alumina: Formation of chlorides. *Applied Catalysis B: Environmental* **2017**, *200*, 274−282.

(11) Chen, L.; Xu, Y.; Sun, Y. Combination of Coagulation and Ozone Catalytic Oxidation for Pretreating Coking Wastewater. *Int. J. Environ. Res. Public Health* **2019**, *16* (10), 1705.

(12) Garcia-Segura, S.; Ocon, J. D.; Chong, M. N. Electrochemical oxidation remediation of real wastewater effluents — A review. *Process Safety and Environmental Protection* **2018**, *113*, 48−67.

(13) Vural, C.; Vural, C.; Ozdemir, G. Monitoring of the degradation of aromatic hydrocarbons by bioaugmented activated sludge. *J. Chem. Technol. Biotechnol.* **2020**, *95* (1), 52−62.

(14) Perez, K.; Toro, N.; Jeldres, M.; Galvez, E.; Robles, P.; Alvarado, O.; Toledo, P. G.; Jeldres, R. I. Estimating the Shear Resistance of Flocculated Kaolin Aggregates: Effect of Flocculation Time, Flocculant Dose, and Water Quality. *Polymers (Basel)* **2022**, *14* (7), 1381.

(15) Liberman, B.; Eshed, L.; Greenberg, G. Pulse Flow RO - The new RO technology for waste and brackish water applications. *Desalination* **2020**, *479*, 114336.

(16) Shi, Q.; Sterbinsky, G. E.; Prigiobbe, V.; Meng, X. Mechanistic Study of Lead Adsorption on Activated Carbon. *Langmuir* **2018**, *34* (45), 13565−13573.

(17) Lachheb, H.; Puzenat, E.; Houas, A.; Ksibi, M.; Elaloui, E.; Guillard, C.; Herrmann, J.-M. Photocatalytic degradation of various types of dyes (Alizarin S, Crocein Orange G, Methyl Red, Congo Red,

Methylene Blue) in water by UV-irradiated titania. *Applied Catalysis B: Environmental* **2002**, *39*, 75.

(18) Zhang, S.; Wang, L.; Zhang, Y.; Cao, F.; Sun, Q.; Ren, X.; Wennersten, R. Effect of hydroxyl functional groups on SO2 adsorption by activated carbon. *Journal of Environmental Chemical Engineering* **2022**, *10* (6), 108727.

(19) Cordero-Lanzac, T.; Rosas, J. M.; García-Mateos, F. J.; Ternero-Hidalgo, J. J.; Palomo, J.; Rodríguez-Mirasol, J.; Cordero, T. Role of different nitrogen functionalities on the electrochemical performance of activated carbons. *Carbon* **2018**, *126*, 65−76.

(20) Arcibar-Orozco, J. A.; Acosta-Herrera, A. A.; Rangel-Mendez, J. R. Simultaneous desulfuration and denitrogenation of model diesel fuel by Fe-Mn microwave modified activated carbon: Iron crystalline habit influence on adsorption capacity. *Journal of Cleaner Production* **2019**, *218*, 69−82.

(21) Cui, Z.; Marcelle, S. s. a.; Zhao, M.; Wu, J.; Liu, X.; Si, J.; Wang, Q. Thermoplastic polyurethane/titania/polydopamine (TPU/TiO2/PDA) 3-D porous composite foam with outstanding oil/water separation performance and photocatalytic dye degradation. *Advanced Composites and Hybrid Materials* **2022**, *5* (4), 2801−2816.

(22) Xie, K.; Wei, S.; Alhadhrami, A.; Liu, J.; Zhang, P.; Elnaggar, A. Y.; Zhang, F.; Mahmoud, M. H. H.; Murugadoss, V.; El-Bahy, S. M.; Wang, F.; Li, C.; Li, G. Synthesis of CsPbBr3/CsPb2Br5@silica yolk-shell composite microspheres: precisely controllable structure and improved catalytic activity for dye degradation. *Advanced Composites and Hybrid Materials* **2022**, *5* (2), 1423−1432.

(23) Meena, P. L.; Poswal, K.; Surela, A. K.; Saini, J. K. Synthesis of graphitic carbon nitride/zinc oxide (g-C3N4/ZnO) hybrid nano-structures and investigation of the effect of ZnO on the photo-degradation activity of g-C3N4 against the brilliant cresyl blue (BCB) dye under visible light irradiation. *Advanced Composites and Hybrid Materials* **2023**, *6* (1), 16.

(24) Chen, C.-Y.; Tseng, C.-C. Two-dimensional Ga2S3/g-C3N4 heterojunction composites with highly enhanced photocatalytic activity and stability. *Advanced Composites and Hybrid Materials* **2023**, *6* (1), 20.

(25) Jiang, X.; Chen, S.; Zhang, X.; Qu, L.; Qi, H.; Wang, B.; Xu, B.; Huang, Z. Carbon-doped flower-like Bi2WO6 decorated carbon nanosphere nanocomposites with enhanced visible light photo-catalytic degradation of tetracycline. *Advanced Composites and Hybrid Materials* **2023**, *6* (1), 9.

(26) Liu, L.; Chen, P.; Zhang, X.; Kovarik, L.; De Yoreo, J. J.; Liu, J.; Sushko, M. L. Solution synthesis of two-dimensional zinc oxide (ZnO)/molybdenum disulfide (MoS2) heterostructure through reactive templating for enhanced visible-light degradation of rhod-amine B. *Advanced Composites and Hybrid Materials* **2023**, *6* (6), 223.

(27) Yi, Z.; Ye, J.; Kikugawa, N.; Kako, T.; Ouyang, S.; Stuart-Williams, H.; Yang, H.; Cao, J.; Luo, W.; Li, Z.; Liu, Y.; Withers, R. L. An orthophosphate semiconductor with photooxidation properties under visible-light irradiation. *Nat. Mater.* **2010**, *9* (7), 559−64.

(28) Duan, Y.; Deng, L.; Shi, Z.; Zhu, L.; Li, G. Assembly of graphene on Ag3PO4/AgI for effective degradation of carbamazepine under Visible-light irradiation: Mechanism and degradation pathways. *Chemical Engineering Journal* **2019**, *359*, 1379−1390.

(29) Han, L.; Yue, X.; Wen, L.; Zhang, M.; Wang, S. A Novel Vermiculite/TiO(2) Composite: Synergistic Mechanism of Enhanced Photocatalysis towards Organic Pollutant Removal. *Molecules* **2023**, *28* (17), 6398.

(30) Casasanta, G.; Falcini, F.; Garra, R. Beer-Lambert law in photochemistry: A new approach. *J. Photochem. Photobiol., A* **2022**, *432*, 114086.

(31) Wu, X.; Liu, K.; Ding, J.; Zheng, B.; Gao, F.; Qian, K.; Ma, Y.; Feng, Y.; Chen, L.; Zhang, P.; Wang, H. Construction of Ni-based alloys decorated sucrose-derived carbon hybrid towards: effective microwave absorption application. *Advanced Composites and Hybrid Materials* **2022**, *5* (3), 2260−2270.

(32) Zeng, J.; Xie, W.; Zhou, H.; Zhao, T.; Xu, B. B.; Jiang, Q.; Algadi, H.; Zhou, Z.; Gu, H. Nitrogen-doped graphite-like carbon derived from phthalonitrile resin with controllable negative magneto-

resistance and negative permittivity. *Advanced Composites and Hybrid Materials* **2023**, *6* (2), 64.

(33) Xu, Y.; Li, W.; Xu, T.; Wang, G.; Huan, W.; Si, C. Straightforward fabrication of lignin-derived carbon-bridged graphitic carbon nitride for improved visible photocatalysis of tetracycline hydrochloride assisted by peroxymonosulfate activation. *Advanced Composites and Hybrid Materials* **2023**, *6* (6), 197.

(34) Shi, C.; An, Y.; Gao, G.; Xue, J.; Algadi, H.; Huang, Z.; Guo, Z. Insights into Selective Glucose Photoreforming for Coproduction of Hydrogen and Organic Acid over Biochar-Based Heterojunction Photocatalyst Cadmium Sulfide/Titania/Biochar. *ACS Sustainable Chem. Eng.* **2024**, *12* (7), 2538−2549.

(35) Nandanwar, R.; Bamne, J.; Singh, N.; Sharma, P. K.; Singh, P.; Umar, A.; Haque, F. Z. Synthesis of Titania/Silica Nanocomposite for Enhanced Photodegradation of Methylene Blue and Methyl Orange Dyes under UV and Mercury Lights. *ES Materials & Manufacturing* **2022**, *16*, 78.

(36) Zheng, J.; Zhang, Y.; Jing, C.; Zhang, H.; Shao, Q.; Ge, R. A visible-light active p-n heterojunction ZnO/Co3O4 composites supported on Ni foam as photoanode for enhanced photo-electrocatalytic removal of methylene blue. *Advanced Composites and Hybrid Materials* **2022**, *5* (3), 2406−2420.

(37) Lu, J.; Wang, Y.; Liu, F.; Zhang, L.; Chai, S. Fabrication of a direct Z-scheme type WO3/Ag3PO4 composite photocatalyst with enhanced visible-light photocatalytic performances. *Appl. Surf. Sci.* **2017**, *393*, 180−190.

(38) Li, X.; Xu, P.; Chen, M.; Zeng, G.; Wang, D.; Chen, F.; Tang, W.; Chen, C.; Zhang, C.; Tan, X. Application of silver phosphate-based photocatalysts: Barriers and solutions. *Chemical Engineering Journal* **2019**, *366*, 339−357.

(39) Lin, Y.; Wu, S.; Li, X.; Wu, X.; Yang, C.; Zeng, G.; Peng, Y.; Zhou, Q.; Lu, L. Microstructure and performance of Z-scheme photocatalyst of silver phosphate modified by MWCNTs and Cr-doped SrTiO3 for malachite green degradation. *Applied Catalysis B: Environmental* **2018**, *227*, 557−570.

(40) Zhang, H.; Chen, B.; Banfield, J. F. The size dependence of the surface free energy of titania nanocrystals. *Phys. Chem. Chem. Phys.* **2009**, *11* (14), 2553−8.

(41) Hwang, S. Y.; Lee, G. B.; Kim, H.; Park, J. E. Influence of mixed methods on the surface area and gas products of activated carbon. *Carbon Letters* **2020**, *30* (6), 603−611.

(42) Li, W.; Zhang, Q.; Zhang, J.; Zheng, Y.; Zhang, H.; Liu, J.; Cui, Y. Fabrication of hydrophobic regenerated activated carbon with high specific surface area. *J. Mater. Sci.* **2021**, *56* (36), 19969−19982.

(43) Ma, Z.-W.; Zhang, K.-N.; Zou, Z.-J.; Lü, Q.-F. High specific area activated carbon derived from chitosan hydrogel coated tea saponin: One-step preparation and efficient removal of methylene blue. *Journal of Environmental Chemical Engineering* **2021**, *9* (3), 105251.

(44) Chen, J.; Lin, Y.; Liu, J.; Wu, D.; Bai, X.; Chen, D.; Li, H. Outstanding supercapacitor performance of nitrogen-doped activated carbon derived from shaddock peel. *Journal of Energy Storage* **2021**, *39*, 102640.

(45) Ding, J.; Rahman, O. u.; Peng, W.; Dou, H.; Yu, H. A novel hydroxyl epoxy phosphate monomer enhancing the anticorrosive performance of waterborne Graphene/Epoxy coatings. *Appl. Surf. Sci.* **2018**, *427*, 981−991.

(46) Zhang, B.-B.; Lin, J.; Song, X.-N.; Wang, C.-K.; Hua, W.; Ma, Y. Identification of oxidation states in γ-graphyne by computational XPS and NEXAFS spectra. *Appl. Surf. Sci.* **2023**, *609*, 155134.

(47) Sulaeman, U.; Hermawan, D.; Andreas, R.; Abdullah, A. Z.; Yin, S. Native defects in silver orthophosphate and their effects on photocatalytic activity under visible light irradiation. *Appl. Surf. Sci.* **2018**, *428*, 1029−1035.

(48) Wu, H.; Wang, Z.-M.; Koike, K.; Negishi, N.; Jin, Y. Hybridization of silver orthophosphate with a melilite-type phosphor for enhanced energy-harvesting photocatalysis. *Catalysis Science & Technology* **2017**, *7* (17), 3736−3746.

(49) Al-Zaban, M. I.; Mahmoud, M. A.; AlHarbi, M. A. Catalytic degradation of methylene blue using silver nanoparticles synthesized by honey. *Saudi J. Biol. Sci.* **2021**, *28* (3), 2007−2013.

(50) Raza, N.; Raza, W.; Gul, H.; Azam, M.; Lee, J.; Vikrant, K.; Kim, K.-H. Solar-light-active silver phosphate/titanium dioxide/silica heterostructures for photocatalytic removal of organic dye. *Journal of Cleaner Production* **2020**, *254*, 120031.

(51) Li, R.; Chen, J.; Cesario, T. C.; Wang, X.; Yuan, J. S.; Rentzepis, P. M. Synergistic reaction of silver nitrate, silver nanoparticles, and methylene blue against bacteria. *Proc. Natl. Acad. Sci. U. S. A.* **2016**, *113* (48), 13612−13617.